Nanoscale

PAPER

View Article Online
View Journal | View Issue

Cite this: *Nanoscale*, 2017, **9**, 9581

Crumpled sheets of reduced graphene oxide as a highly sensitive, robust and versatile strain/pressure sensor†

Subhajit Kundu, [a] Rammohan Sriramdas,[b] Kazi Rafsanjani Amin, [c] Aveek Bid, [c] Rudra Pratap[b] and Narayanan Ravishankar *[a]

Received 5th April 2017,
Accepted 8th June 2017

DOI: 10.1039/c7nr02415k

rsc.li/nanoscale

Sensing of mechanical stimuli forms an important communication pathway between humans/environment and machines. The progress in such sensing technology has possible impacts on the functioning of automated systems, human machine interfacing, health-care monitoring, prosthetics and safety systems. The challenges in this field range from attaining high sensitivity to extreme robustness. In this article, sensing of complex mechanical stimuli with a patch of taped crumpled reduced graphene oxide (rGO) has been reported which can typically be assembled under household conditions. The ability of this sensor to detect a wide variety of pressures and strains in conventional day-to-day applications has been demonstrated. An extremely high gauge factor (~10^3) at ultralow strains (~10^{-4}) with fast response times (<20.4 ms) could be achieved with such sensors. Pressure resulting from a gentle touch to over human body weight could be sensed successfully. The capability of the sensor to respond in a variety of environments could be exploited in the detection of water and air pressures both below and above atmospheric, with a single device.

Introduction

Sensing of strain is important in day-to-day life for the functioning of automated systems, human machine interfacing, prosthetics, health-care monitoring and security applications.[1–6] Typically, electronic strain sensors are based on the principle of force-induced changes in resistance, capacitance, piezoelectricity or triboelectricity.[1,7–12] Of these, resistance-based sensors are particularly interesting due to the simplicity in their electronics and their low power consumption. Percolation networks, in which force-induced pathways are created for the flow of current, have largely been utilized in this regard.[13–18] The basic strategy has been shown to use a dispersion of conducting nanomaterials like Au/Ag nanowires or carbon nanotubes in/on a non-conducting polymer matrix making the device highly stretchable and hence wearable.[5,19–22] Other strategies involved the use of aligned carbon nanotube arrays,[1] Au nanowire patches on polymers,[23] or reversible interlocking of nanofibers.[2] More recently, a very high gauge factor could be achieved by some methods.[24–26] However, only limited success has been achieved using these techniques for the detection of ultra-low strains (~10^{-4}) with a high gauge factor (>10^3) (ESI, Table S1†).

Sensors need to be able to respond to small hydrostatic stresses to qualify as pressure sensors. Several protocols have been employed to develop pressure sensors that show human skin like sensitivity and flexibility.[4,27–35] High sensitivity at low pressure could be achieved by various methods.[25,36,37] Simple strategies like Au-nanowire-impregnated tissue paper,[15] conductor-dispersed rubber,[38] and laser-scribed graphene[39,40] have been investigated that show good promise for detection in a low-pressure range. However, pressure sensors that involve simple fabrication steps, are highly sensitive over a wide range of pressures and are mechanically robust are still elusive.

Chemically-reduced graphene-oxide (rGO) offers superior conductivity with excellent flexibility and hence has been utilized in the design of percolation-network-based pressure/strain sensors.[13,32,41,42] In all these studies, the basic idea has been to space out the conducting medium using complicated natural/artificial microstructuring. Recently, it has been shown that 2-dimensional sheet-like flexible nanomaterials, such as graphene, dispersed in a liquid medium undergo paper-like crumpling on drying due to the capillary forces exerted by the

[a]*Materials Research Centre, Indian Institute of Science, Bangalore, 560012, India. E-mail: nravi@mrc.iisc.ernet.in*
[b]*Centre for Nano Science and Engineering, Indian Institute of Science, Bangalore, 560012, India*
[c]*Department of Physics, Indian Institute of Science, Bangalore, 560012, India*

†Electronic supplementary information (ESI) available: Details of the synthesis of materials and fabrication of the sensor; experimental and theoretical procedures adopted for strain and pressure sensing; and supporting videos. See DOI: 10.1039/c7nr02415k

solvent.[43–46] Such crumpled graphene offers a very loose packing of a highly compressible matrix and hence is a potential candidate for designing ultrasensitive strain/pressure sensors.

Here we demonstrate a simple and novel strategy for sensing a variety of stress/strain states using crumpled rGO sheets drop-cast and confined on a substrate. Fig. 1a demonstrates the typical fabrication steps involved in the realization of the reduced graphene oxide (rGO) strain/pressure sensor (details are given in the ESI†). Two different geometries of the device were fabricated, which have implications as discussed later – fully confined rGO (fc-rGO) and partially confined rGO (pc-rGO). Sensing of strains of the order 10^{-4} using a vibrating cantilever could be achieved with an ultrahigh gauge factor of >4000. The measurement of strains at a frequency of as high as 49 Hz has been shown indicating an ultrafast switching time of about 20.4 ms. A minor modification in the device fabrication enables measurement of high pressures (>3 MPa) with outstanding stability. The simplicity of device fabrication enables realization of sensors with different geometries for measuring impact forces, and water pressure and air pressure both above and below the atmospheric pressure with sensitivity as high as 4170 kPa^{-1} in the low-pressure regime.

Experimental

Synthesis of rGO

For the synthesis of rGO, first GO has been synthesized by Hummer's method.[47] Concentrated H_2SO_4 (23 ml) was placed in a beaker and cooled to 0 °C by placing the beaker in an ice bath. $KMnO_4$ (3 g) was added to it while stirring. The mixture was kept under stirring for 30 minutes after which deionized (d.i.) H_2O (45 ml) was added to it. The temperature increases with the addition of H_2O that is maintained for 15 more minutes. The reaction was terminated by addition of H_2O (140 ml) followed by addition of H_2O_2 (10 ml of 30% v/v). The sample was then washed with 5% HCl solution. Complete removal was checked at every cleaning step by addition of $BaCl_2$ to the supernatant. Then the sample was washed a few times with acetone and dried in air overnight.

rGO has been synthesized by reduction of GO in water at a high temperature.[48] In a typical synthesis, dried GO powder (100 mg) was dispersed in d.i. water (15 ml) by ultrasonication. Microwave heating of the mixture was done under closed vessel conditions at 200 °C for an hour. The product was washed a few times with water and then finally with acetone. The settled final product was left overnight for drying.

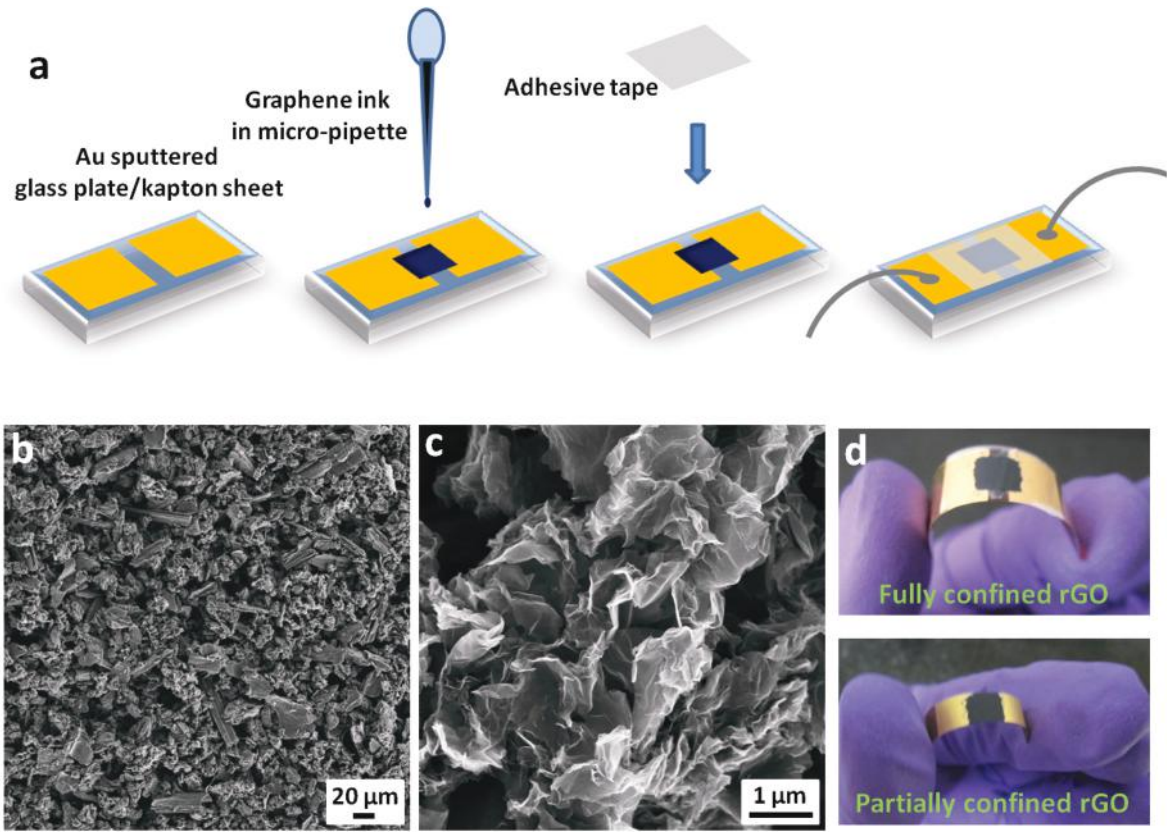

Fig. 1 (a) Schematic showing the fabrication process of a taped rGO strain/pressure sensor. (b), (c) SEM images at low/high magnification showing the crumpled state of dropcast rGO. (d) Photograph of the fabricated devices in two different geometries – fully confined rGO and partially confined rGO.

Fabrication of a sensor

The obtained rGO powder was dispersed in acetone to form a thick ink (typically about 2 mg of rGO in 50 μL of acetone) and subsequently dropcast in between sputtered Au contacts (separated by 2 mm) on a Kapton sheet (2.5 cm × 1 cm) to form a uniform layer. An area (A) of 0.5 × 0.5 cm^2 was defined by removing the excess rGO powder from the edges. Typically a resistance of less than 10 kΩ was observed after drying of the rGO powder. An SEM image of the concentrated ink after drying was obtained by dropcasting it on a Si wafer (Fig. 1b and c). It shows a highly aggregated but loosely packed and crumpled-up state of the rGO indicating poor contact between the rGO flakes initially. The dried powder was taped with adhesive tape (scotch tape, 3m; thickness 60 μm, Young's modulus: 1.1 GPa). On taping, compression happens, which leads to lowering of the off-resistance (fc-rGO device). The Kapton sheet was subsequently cut from both sides to free the sides of the adhesive tape on both sides of the rGO aggregate (pc-rGO device) resulting in a device dimension of 2.5 cm × 0.5 cm. A slight increase in the off-resistance (R_0) was observed due to partial release of the compression from the sides. The two kinds of devices are shown in Fig. 1d.

Results and discussion

The sensor pc-rGO was placed over a steel/copper cantilever and the end of the cantilever was given discrete displacements (1–4 mm in steps of 1 mm) to strain the beam (refer schematic in Fig. 2a). The strain (δ) at the sensing element for each case was calculated using cantilever bending theory (details are given in the ESI†). A constant voltage was applied to the sensor and the corresponding current was recorded as the cantilever was strained. Fig. 2b shows the variation of the resistance R of the sensor with strain considering the tensile strain of the device (downward bending of the cantilever) as positive and compressive strain (upward bending) as negative. The data are plotted as $\Delta R/R_0$ where, $\Delta R = R_0 - R$, R_0 being the resistance of the sensor in the unstrained state. It was observed that while there was a decrease in resistance under tensile strain of the cantilever, the resistance increased during the compressive straining cycle. The cross-sectional imaging of the taped rGO using an optical microscope under the strained conditions showed (ESI, Fig. S3†) that the cross-sectional area reduced under tensile straining of the device indicating compression of the crumpled rGO aggregates. This led to better electrical contact formation among the rGO flakes resulting in the reduced resistance of the device. In the opposite scenario, the reduction of contact between the rGO flakes during the compressive cycle led to an increase in the resistance. The relative increase in resistance observed during the compression part of the cycle was much higher than the relative decrease observed during the tensile part of the cycle. To understand this phenomenon, $\Delta R/R_0$ was computed using the standard percolation theory.[49,50] The theoretical plot of $\Delta R/R_0$ *vs.* strain (inset of Fig. 2b) shows a trend quite similar to that observed experimentally (details are given in ESI, section III.III†) lending credence to our understanding of the observed phenomenon.

The figure of merit of a strain sensor, *i.e.* the gauge factor (GF) is quantified using the expression $(\Delta R/R_0)/\delta$. The calculated GF for the pc-rGO device as a function of the applied strain is shown in Fig. 2c. For positive strains, the GF is

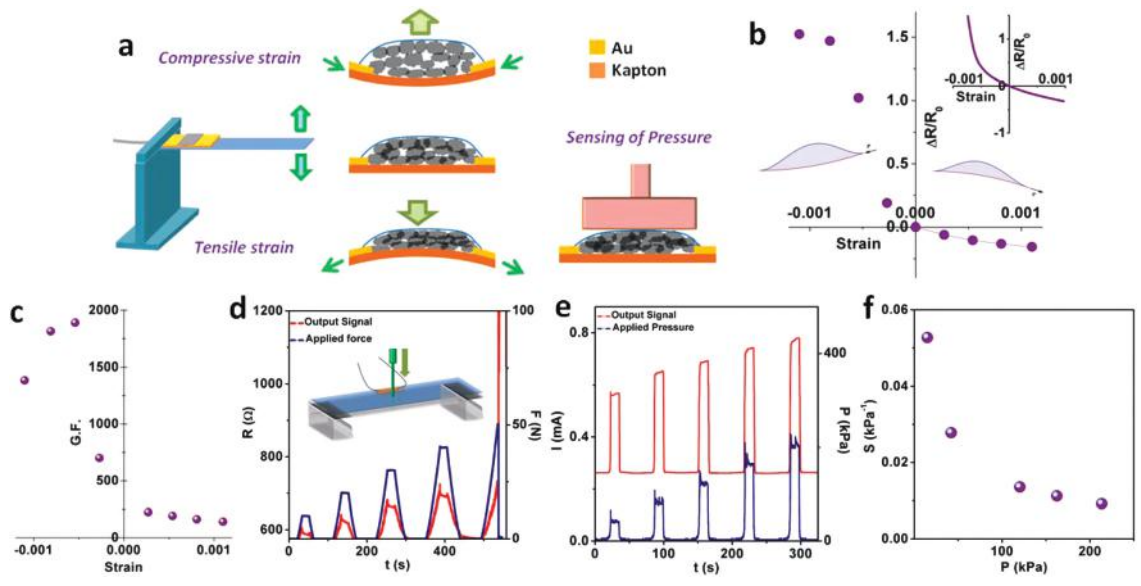

Fig. 2 (a) Schematic showing the configuration of the crumpled rGO aggregate during the detection of strain and pressure. (b) Relative change in the resistance of a typical pc-rGO sensor in response to strain in the cantilever. Inset shows the simulated relative change in the resistance of the rGO aggregate. An excellent agreement between the experiments and simulation is observed. (c) Corresponding gauge factor as a function of strain. (d) Detection of deformation in glass (before breaking) because of the application of a force at its centre. Inset describes the experimental set-up. (e) Current response of a similar pc-rGO sensor to applied pressure. (f) Variation of the sensitivity of the sensor with applied pressure.

nominal and decreases at higher strains due to exhaustion of the possible contact points for higher compression of the rGO flakes. However, for negative strains the GF reached as high a value as 1891 at a strain of 5.4×10^{-4} and then decreased with further increase in the strain. This observation suggests a progressive loosening of contacts that occurs with increasing compressive strain until the rGO assembly no longer feels the constraints of the adhesive tape and is in a fully relaxed state. The upper limit to the strain at which the GF is maximum is set by the conditions beyond which there is no more increase in the contact area as the strain is increased.

The ability of a sensor to detect ultra-low strains ($\sim 10^{-4}$) has direct implications in structural health monitoring. Glass is a typical brittle material and undergoes minimal plastic deformation before it fractures and hence was chosen as a model system for the measurement of low strains. The rGO sensor (pc-rGO) was integrated on a glass slide; the relative positions of the supports, the sensor, and the application of loads are shown in the inset of Fig. 2d. The load was applied using a flat punch with an area of 2 mm × 1 mm at the centre of the glass slide (away from the sensor) and the deformation and the corresponding current response of the sensor were recorded. Application of the load increased the resistance (Fig. 2d) of the sensor indicating straining of the sensor, which in turn implied straining of the glass slide. A strain in the glass as small as 4.6×10^{-4} at a load of 10 N could be detected successfully with the sensor. With increasing load in the subsequent cycles, the change in the resistance also increased confirming that the change in R was caused by the progressive bending of the glass. At about 50 N force, the glass broke leading to extensive bending of the sensor resulting in a drastic increase in its resistance.

The piezoresistive nature of the crumpled rGO aggregate could also be applied for sensing of pressures. Fig. 2e shows the current I response of a pc-rGO device to pulsed pressure P. As the magnitude of the pressure pulse increased, an increase in I was observed due to compression of the rGO aggregate in the transverse direction, as was observed in the case of tensile straining of the device on the cantilever. The evaluation of the sensitivity S of the pressure sensor was done using the standard formula, $S = (\Delta I/I_0)/P$. The plot of the sensitivity *vs.* pressure (Fig. 2f) shows that it was the highest at lower pressures and progressively tended to saturate at higher pressures. Such a phenomenon could be due to exhaustion at a higher load of the possible contact points between the crumpled rGO flakes. To visualize the change in rGO packing with compression, optical microscopy imaging (ESI, Fig. S7†) of rGO sandwiched between the two glass slides was carried out as a function of load. At low loads, the flakes showed poor contact among each other and hence the device was highly resistive. On gradually increasing the load, we observed improvement in the contact between the rGO grains leading to a lowering of the device resistance. But the rate of increase of the contact area between the flakes with pressure dropped at higher loads which is the main reason for lower sensitivity at higher pressures.

To investigate its dynamic response, the sensor (pc-rGO) was mounted on a cantilever and was set to vibrate (experimental details are given in the ESI†). Fig. 3a shows the change in the resistance of the sensor with time and the corresponding change in the velocity of the cantilever tip which is an indirect measure of the strain. An excellent readout of ultrafast switching of strain could be obtained. With increasing frequency, the velocity (hence the strain) reached a maximum at around 28 Hz which is the resonant frequency of the cantilever. The response of the sensor at 28 Hz along with the computed strain is shown in Fig. 3b. The change in the resistance was found to scale with the strain. A gauge factor as high as 4282 could be obtained at a strain of -1.8×10^{-4}. The evaluation of the device over >7000 cycles at a frequency of 33 Hz showed an extremely consistent performance at such a high frequency (Fig. 3c). A successful readout of strains at a frequency of as high as 49 Hz (Fig. 3d) could be obtained. This indicates that the sensor has a fast switching time of <20.4 ms even at such low strain levels.

As an application of the excellent dynamic response of the sensor, we demonstrate the recording of sound that involves detection of dynamic pressure pulses as small as ~1 Pa at high frequencies.[33] For this purpose, the strain sensor (pc-rGO) was pasted on a thin tissue paper membrane fixed over a beaker as shown in the inset of Fig. 3e. A piece of music was played with a speaker placed at a distance of 10 cm from the sensor and the corresponding current response of the sensor was recorded. The whole system including the speaker and the beaker was placed on a soft tissue bed to prevent any transmission of vibration through the table. Gentle tapping of the speaker did not lead to any significant change in the resistance of the device ensuring sufficient isolation and thus the response of the sensor was ensured to be solely due to the vibration passing through the intervening air medium. As shown in Fig. 3e, the vibrations due to the small changes in the air pressure were captured by the sensor with high fidelity (refer ESI Video MVI 1†). The quantification of the sound intensity of the played music at 50% volume and at a distance of 10 cm shows that the sensor is capable of detecting acoustic vibrations of intensity about 80–85 dB. Such high sensitivity at low amplitudes from a distant source has implications in designing hearing aids and efficient microphones.

Post detection of low strain/pressure, the rGO sheets recover completely and return to their original unstrained state. However, for large pressures, there is a significant drift in the base current (ESI, Fig. S9†) due to the irreversible rearrangement of the rGO flakes. This was found to be a direct result of the geometry of the sensor (pc-rGO) in which the rGO flakes are not completely confined within the adhesive tape and can leak from the sides where there is no constraint from the tape. Thus, this geometry is unsuitable for the detection of higher strains. Secure taping of the rGO flakes from the sides could be an alternative to design sensors with stable and extended strain sensing capabilities. Also, for accurate measurement in the high strain regime, a rigid substrate would be beneficial. Hence, a modified device architecture was

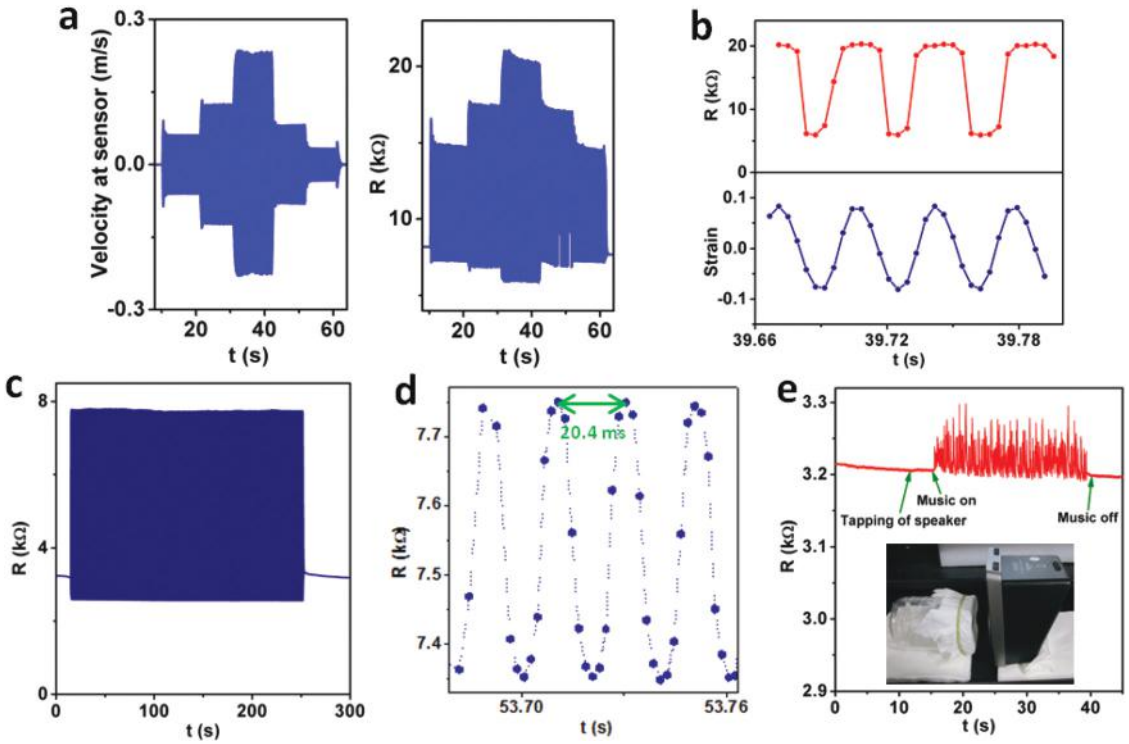

Fig. 3 (a) Plot of the velocity of the tip of the cantilever and the corresponding changes in the resistance of the sensor as the vibration frequency of the cantilever was varied (26–30 Hz in steps of 1 Hz) around the resonance frequency of the cantilever. (b) Variation of resistance and strain with time at a frequency of 28 Hz. (c) Plot showing the cycling stability of the sensor for >7000 cycles at 33 Hz. (d) Ultrafast switching time of ~20.4 ms corresponding to a strain frequency of 49 Hz. (e) Response of the sensor to acoustic vibrations. Inset shows the photograph of the measurement set-up.

developed using the same protocol as described earlier but on a rigid glass substrate and with conformal taping on all sides of the drop-cast rGO aggregate. This geometry is designated as the fully constrained geometry (fc-rGO) as opposed to the partially confined geometry (pc-rGO) described earlier. The current response of such an fc-rGO sensor for pressures up to ~3.6 MPa is shown in Fig. 4a. No significant drift in the base current was seen even after 5 cycles indicating that this form of the device enables detection of high pressure with good stability (ESI, Fig. S10†). However, at a higher loading, the current response becomes sluggish for a fixed approach rate (1 mm s^{-1}) indicating the pressure-dependent inelastic nature of the crumpled rGO aggregate.

Careful observation of the current response of the sensor (fc-rGO) revealed that as the pressure was slowly increased, the current initially decreased and after crossing a certain threshold pressure, started increasing. The same behavior was observed as the load was reduced to zero. This is counter-intui-

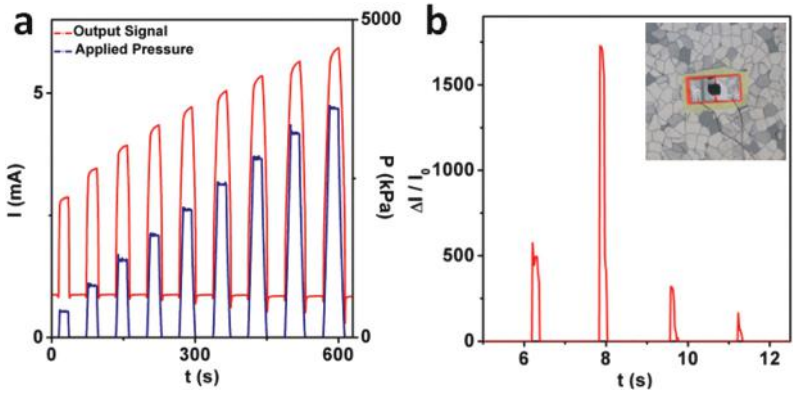

Fig. 4 (a) Stable response of a fully confined rGO device to high pressures. The blue curves are the applied pressures and the orange curve is the current output of the device in response to the pressure. (b) Response of the adhesive label based sensor pasted on a floor (inset) for hammering showing that it is extremely robust.

tive and is contrary to the expectation that an increase in pressure should lead always to a decrease in *R*. Control experiments (details are given in in ESI, section V.III†) indicated that this anomaly was due to the presence of trapped air under the tape in the case of the fully confined geometry of the rGO. Although pressing the sensor at a given location leads to a compression of the rGO flakes locally (thus reducing the resistance locally), it also leads to the trapped air expanding in the adjacent regions leading to an initial increase in the resistance. This was validated by either puncturing or cutting the sides of the tape (ESI, Fig. S13†). In this case, the trapped air was able to escape on application of the pressure and consequently, the initial increase in *R* is not seen. A comparison of the sensitivity of the two kinds of devices (fully constrained fc-rGO *versus* the partially constrained pc-rGO) revealed that the sensitivity of the partially confined device was higher than that of the fully constrained one. Partial release of the constraints initially leads to a higher off-resistance of the same device compared to the fully constrained case due to the partial relaxation of the rGO flakes, thus leading to higher sensitivity. Thus it appears that reducing the confinement of rGO is key to designing sensors with higher sensitivity. To further validate this hypothesis, we conducted experiments on a glass-based sensor with the rGO confined using an increasing number of layers of adhesive tape. Increasing the number of layers of adhesive tape on the same device caused increased initial compression (lowering of the off-resistance) of the rGO aggregate leading to exhaustion of the possible contact points between the rGO flakes resulting in poorer sensitivity.

The evaluation of the performance of the pc-rGO sensor at a lower bias voltage of 1 mV and current of few μA (ESI, Fig. S15†) shows that it has an excellent signal-to-noise ratio even at a power as low as a few nanowatts.

The simplicity of device fabrication allows it to be directly integrated on virtually any surface. As an example, fabrication of the device (fc-rGO) is demonstrated on adhesive labels that can be easily pasted on any surface (inset of Fig. 4b). Hard pressing, stamping with foot and even hammering shocks (Fig. 4b, also refer ESI Video MVI 2†) do not alter the base resistance indicating that this form of the device is extremely robust and has potential for use in designing smart floor mats. Quantifiable experiments with an impact hammer indicate that indeed it can measure impact forces of short duration with ultrafast recovery (ESI, Fig. S16†). Measurement under increasing load (load cells used) shows that it can withstand forces as large as a few kN (>100 kg on earth). To further test the measurement potential at higher loads, experiments were conducted with pulsed loads. It is observed that a pressure of the order of 40 MPa could be measured with instant recovery. With increasing load, the response became progressively sluggish and finally led to device damage at ~80 MPa. The damage was primarily seen to be due to the failure of the tape/label/contacts that leads to spreading out of the rGO flakes.

The fully constrained geometry (fc-rGO device) offers a unique advantage of usability of the device under water for the detection of water pressure. To demonstrate this, the sensor was dipped to different depths into a beaker filled with water (Fig. 5a) and the current response was recorded. Alternating dipping cycles between depths of 3 cm (0.3 kPa) to 28 cm (2.7 kPa) produced the current profile shown in Fig. 5b (also refer ESI Video MVI 3†) indicating the suitability of the device as a hydrostatic pressure sensor. In principle, the response of the

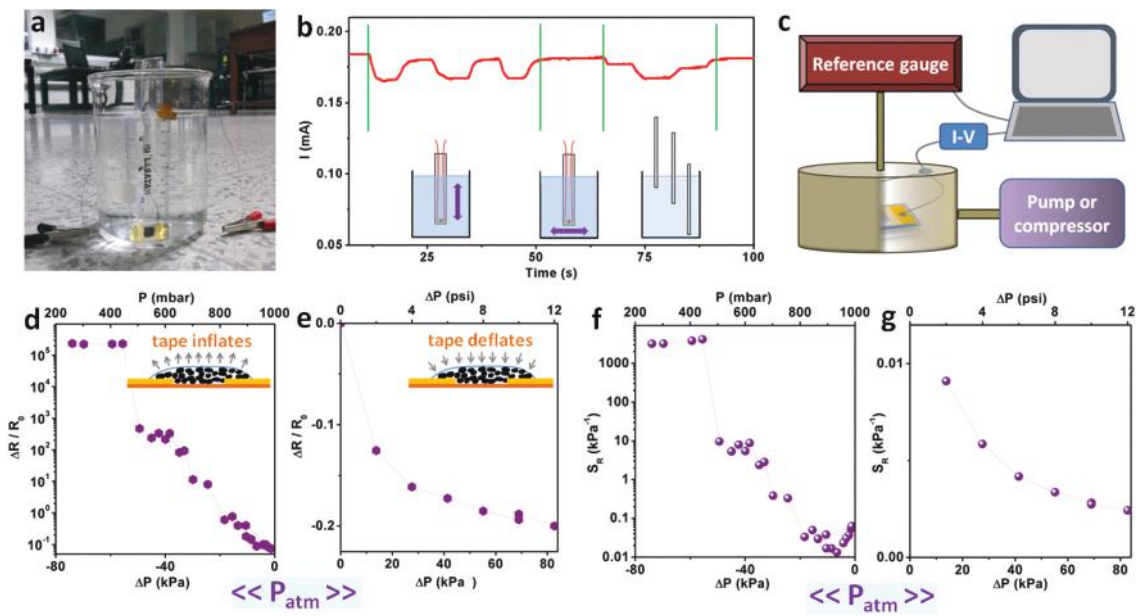

Fig. 5 (a) Photograph showing the sensor pasted on a scale dipped in a beaker full of water. (b) Current response of the sensor to changes in depth of the sensor in water. (c) Schematic showing the set-up for detection of air pressure. (d), (e) Relative change in the resistance of the sensor at pressures lower than and higher than the atmospheric pressures respectively. Schematics in the inset showing that the rGO-tape inflates/deflates when the pressure changes to a value below/above the atmospheric pressure. (f), (g) Corresponding variation in the sensitivity of the sensor.

sensor to turbulence in water could lead to false interpretation of the pressure due to a change in the depth. To investigate this effect, the device was moved randomly horizontally while maintaining the same depth. The effect of turbulence on the response of the device was observed to be negligible compared to that of the water pressure making it suitable for unambiguous detection of fluid pressure.

The experiments described above also indicate that the sensor could be used for the detection of air pressure/vacuum. The sensor integrated on a glass slide was enclosed in a sealed chamber connected to a Pirani gauge (as a reference) and air was pumped out using a rotary pump (Fig. 5c). The current response of the sensor and the pressure response of the reference gauge were acquired simultaneously (ESI, Fig. S17†). It is observed that the current dropped by more than two orders of magnitude for a typical pressure pulse of ~679 mbar and completely recovered on venting the chamber indicating that the sensor was extremely sensitive. Measurements conducted during successive pumping/venting of the chamber further demonstrate the stability and reproducibility of the device response. The plots of $\Delta R/R_0$ *vs.* ΔP show that with decreasing pressure the resistance increased (Fig. 5d) progressively with a higher change occurring at lower pressures. A change in the current as large as five orders of magnitude was detected at 444 mbar below which the change in the current tended to saturate, possibly due to the stretch limit of the adhesive tape. For positive pressures in the chamber, a decrease in the device resistance is observed (Fig. 5e). This shows the usability of a single device in the detection of air pressure both above and below atmospheric pressure. The percentage change in the resistance at any particular ΔP was significantly lower at pressures above the atmospheric pressure (compression of rGO flakes) as compared to pressures below the atmospheric pressure (expansion of the rGO flakes), consistent with the observation of strain sensing illustrated earlier.

The sensitivity of a resistance based air pressure sensor is defined as, $S_R = (\Delta R/R_0)/\Delta P$. The variation of S_R with ΔP (Fig. 5f and g) was similar to that observed in the case of a gauge factor in strain sensing indicating that the percolation behavior is similar in both these cases. Sensitivity values as high as ~4170 kPa^{-1} could be obtained at a pressure of 444 mbar. The increase in the resistance with reduction of pressure below the atmospheric pressure in this case is due to the inflation of the adhesive tape/rGO system leading to progressive loosening of contact among the rGO flakes (inset of Fig. 5d and e). As expected, the trapped air in the fully constrained geometry plays a key role in the sensitivity of the device (ESI, Fig. S18†).

Conclusions

In conclusion, a very simple and efficient protocol has been developed to fabricate strain sensors with taped crumpled rGO. The detection of ultra-low strain of ~10^{-4} with a gauge factor >4000 has been demonstrated. Ultrafast switching of strain at 49 Hz could be detected implying a response time of 20.4 ms. Consistent performance of the strain sensor over >7000 cycles has been demonstrated. Bending of glass could be detected before breaking which indicates the potential of the sensor for monitoring structural health with high sensitivity. The detection of static pressure has been demonstrated over a wide range of pressures (a few kPa to MPa) ranging from a gentle tapping to over human body weight. The ability of the sensor to withstand hard pressing forces and hammering shocks demonstrated its robustness and has implications for the design of smart mats. Performance under water has been demonstrated by unambiguously detecting water pressure. A unique air trapped arrangement led to the detection of air pressure both below and above the atmospheric pressure with a high sensitivity of ~4170 kPa^{-1} achieved in the low pressure regime. The methodology of fabrication is general and works even with the starting graphite and the pre-synthesized GO, but rGO works the best by virtue of its unique morphology (ESI, Fig. S19†). Further, tuning of the packing[44,51] (compressed/relaxed) of such crumpled conducting sheets of rGO under elastic tape holds promise for improving the efficacy/range in application specific sensor designs.

Acknowledgements

NR acknowledges the Department of Science and Technology (DST), India for financial support. AB acknowledges funding from Nanomission, DST, Govt of India. KRA thanks CSIR, MHRDG, Govt. of India for financial support. We acknowledge the use of instruments in CeNSE and AFMM which are central facilities at IISc.

Notes and references

1 T. Yamada, Y. Hayamizu, Y. Yamamoto, Y. Yomogida, A. Izadi-Najafabadi, D. N. Futaba and K. Hata, *Nat. Nanotechnol.*, 2011, **6**, 296–301.
2 C. Pang, G.-Y. Lee, T.-i. Kim, S. M. Kim, H. N. Kim, S.-H. Ahn and K.-Y. Suh, *Nat. Mater.*, 2012, **11**, 795–801.
3 D. J. Lipomi, M. Vosgueritchian, B. C. K. Tee, S. L. Hellstrom, J. A. Lee, C. H. Fox and Z. Bao, *Nat. Nanotechnol.*, 2011, **6**, 788–792.
4 D.-H. Kim, N. Lu, R. Ma, Y.-S. Kim, R.-H. Kim, S. Wang, J. Wu, S. M. Won, H. Tao, A. Islam, K. J. Yu, T.-i. Kim, R. Chowdhury, M. Ying, L. Xu, M. Li, H.-J. Chung, H. Keum, M. McCormick, P. Liu, Y.-W. Zhang, F. G. Omenetto, Y. Huang, T. Coleman and J. A. Rogers, *Science*, 2011, **333**, 838–843.
5 S. Jung, J. H. Kim, J. Kim, S. Choi, J. Lee, I. Park, T. Hyeon and D.-H. Kim, *Adv. Mater.*, 2014, **26**, 4825–4830.
6 E. Roh, B.-U. Hwang, D. Kim, B.-Y. Kim and N.-E. Lee, *ACS Nano*, 2015, **9**, 6252–6261.
7 D. J. Cohen, D. Mitra, K. Peterson and M. M. Maharbiz, *Nano Lett.*, 2012, **12**, 1821–1825.

8 J. Lee, H. Kwon, J. Seo, S. Shin, J. H. Koo, C. Pang, S. Son, J. H. Kim, Y. H. Jang, D. E. Kim and T. Lee, *Adv. Mater.*, 2015, **27**, 2433–2439.
9 J. Zhou, Y. Gu, P. Fei, W. Mai, Y. Gao, R. Yang, G. Bao and Z. L. Wang, *Nano Lett.*, 2008, **8**, 3035–3040.
10 Y. Yang, H. Zhang, Z.-H. Lin, Y. S. Zhou, Q. Jing, Y. Su, J. Yang, J. Chen, C. Hu and Z. L. Wang, *ACS Nano*, 2013, **7**, 9213–9222.
11 F.-R. Fan, L. Lin, G. Zhu, W. Wu, R. Zhang and Z. L. Wang, *Nano Lett.*, 2012, **12**, 3109–3114.
12 S. Ryu, P. Lee, J. B. Chou, R. Xu, R. Zhao, A. J. Hart and S.-G. Kim, *ACS Nano*, 2015, **9**, 5929–5936.
13 M. Hempel, D. Nezich, J. Kong and M. Hofmann, *Nano Lett.*, 2012, **12**, 5714–5718.
14 R. Rahimi, M. Ochoa, W. Yu and B. Ziaie, *ACS Appl. Mater. Interfaces*, 2015, **7**, 4463–4470.
15 S. Gong, W. Schwalb, Y. Wang, Y. Chen, Y. Tang, J. Si, B. Shirinzadeh and W. Cheng, *Nat. Commun.*, 2014, **5**, 3132.
16 K. K. Kim, S. Hong, H. M. Cho, J. Lee, Y. D. Suh, J. Ham and S. H. Ko, *Nano Lett.*, 2015, **15**, 5240–5247.
17 S. M. Mohanasundaram, R. Pratap and A. Ghosh, *J. Appl. Phys.*, 2012, **112**, 084332–084339.
18 G. Lubineau, A. Mora, F. Han, I. N. Odeh and R. Yaldiz, *Comput. Mater. Sci.*, 2017, **130**, 21–38.
19 F. Xu and Y. Zhu, *Adv. Mater.*, 2012, **24**, 5117–5122.
20 M. Amjadi, A. Pichitpajongkit, S. Lee, S. Ryu and I. Park, *ACS Nano*, 2014, **8**, 5154–5163.
21 N. Lu, C. Lu, S. Yang and J. Rogers, *Adv. Funct. Mater.*, 2012, **22**, 4044–4050.
22 C. S. Boland, U. Khan, C. Backes, A. O'Neill, J. McCauley, S. Duane, R. Shanker, Y. Liu, I. Jurewicz, A. B. Dalton and J. N. Coleman, *ACS Nano*, 2014, **8**, 8819–8830.
23 S. Gong, D. T. H. Lai, B. Su, K. J. Si, Z. Ma, L. W. Yap, P. Guo and W. Cheng, *Adv. Electron. Mater.*, 2015, **1**, 1400063.
24 J. Zhou, H. Yu, X. Xu, F. Han and G. Lubineau, *ACS Appl. Mater. Interfaces*, 2017, **9**, 4835–4842.
25 J. Zhou, X. Xu, H. Yu and G. Lubineau, *Nanoscale*, 2017, **9**, 604–612.
26 Y. Tai and G. Lubineau, *Sci. Rep.*, 2016, **6**, 19632.
27 J. J. Boland, *Nat. Mater.*, 2010, **9**, 790–792.
28 K. Takei, T. Takahashi, J. C. Ho, H. Ko, A. G. Gillies, P. W. Leu, R. S. Fearing and A. Javey, *Nat. Mater.*, 2010, **9**, 821–826.
29 B. C. K. Tee, C. Wang, R. Allen and Z. Bao, *Nat. Nanotechnol.*, 2012, **7**, 825–832.
30 W. Wu, X. Wen and Z. L. Wang, *Science*, 2013, **340**, 952–957.
31 Y. Zang, F. Zhang, D. Huang, X. Gao, C.-A. Di and D. Zhu, *Nat. Commun.*, 2015, **6**, 6269.
32 B. Zhu, Z. Niu, H. Wang, W. R. Leow, H. Wang, Y. Li, L. Zheng, J. Wei, F. Huo and X. Chen, *Small*, 2014, **10**, 3625–3631.
33 Y. Zang, F. Zhang, C.-A. Di and D. Zhu, *Mater. Horiz.*, 2015, **2**, 140–156.
34 S. C. B. Mannsfeld, B. C. K. Tee, R. M. Stoltenberg, C. V. H. H. Chen, S. Barman, B. V. O. Muir, A. N. Sokolov, C. Reese and Z. Bao, *Nat. Mater.*, 2010, **9**, 859–864.
35 Q. Shao, Z. Niu, M. Hirtz, L. Jiang, Y. Liu, Z. Wang and X. Chen, *Small*, 2014, **10**, 1466–1472.
36 Y. Tai, M. Mulle, I. A. Ventura and G. Lubineau, *Nanoscale*, 2015, **7**, 14766–14773.
37 Y. Tai and G. Lubineau, *Adv. Funct. Mater.*, 2016, **26**, 4078–4084.
38 Y. Tang, S. Gong, Y. Chen, L. W. Yap and W. Cheng, *ACS Nano*, 2014, **8**, 5707–5714.
39 H. Tian, Y. Shu, X.-F. Wang, M. A. Mohammad, Z. Bie, Q.-Y. Xie, C. Li, W.-T. Mi, Y. Yang and T.-L. Ren, *Sci. Rep.*, 2015, **5**, 8603.
40 H. Tian, Y. Shu, Y.-L. Cui, W.-T. Mi, Y. Yang, D. Xie and T.-L. Ren, *Nanoscale*, 2014, **6**, 699–705.
41 H.-B. Yao, J. Ge, C.-F. Wang, X. Wang, W. Hu, Z.-J. Zheng, Y. Ni and S.-H. Yu, *Adv. Mater.*, 2013, **25**, 6692–6698.
42 X. Li, P. Sun, L. Fan, M. Zhu, K. Wang, M. Zhong, J. Wei, D. Wu, Y. Cheng and H. Zhu, *Sci. Rep.*, 2012, **2**, 395.
43 X. Ma, M. R. Zachariah and C. D. Zangmeister, *Nano Lett.*, 2012, **12**, 486–489.
44 D. Parviz, S. D. Metzler, S. Das, F. Irin and M. J. Green, *Small*, 2015, **11**, 2661–2668.
45 G. A. Vliegenthart and G. Gompper, *Nat. Mater.*, 2006, **5**, 216–221.
46 J. Luo, H. D. Jang, T. Sun, L. Xiao, Z. He, A. P. Katsoulidis, M. G. Kanatzidis, J. M. Gibson and J. Huang, *ACS Nano*, 2011, **5**, 8943–8949.
47 W. S. Hummers and R. E. Offeman, *J. Am. Chem. Soc.*, 1958, **80**, 1339–1339.
48 C. Nethravathi and M. Rajamathi, *Carbon*, 2008, **46**, 1994–1998.
49 T. Chelidze and Y. Gueguen, *J. Phys. D: Appl. Phys.*, 1998, **31**, 2877.
50 M. Sahimi, *Applications of Percolation Theory*, Taylor & Francis, London, 1994.
51 Y. Wu, N. Yi, L. Huang, T. Zhang, S. Fang, H. Chang, N. Li, J. Oh, J. A. Lee, M. Kozlov, A. C. Chipara, H. Terrones, P. Xiao, G. Long, Y. Huang, F. Zhang, L. Zhang, X. Lepró, C. Haines, M. D. Lima, N. P. Lopez, L. P. Rajukumar, A. L. Elias, S. Feng, S. J. Kim, N. T. Narayanan, P. M. Ajayan, M. Terrones, A. Aliev, P. Chu, Z. Zhang, R. H. Baughman and Y. Chen, *Nat. Commun.*, 2015, **6**, 6141.